Environment International 143 (2020) 105899

Contents lists available at ScienceDirect

Environment International

journal homepage: www.elsevier.com/locate/envint

Singlet oxygen mediated the selective removal of oxytetracycline in C/Fe_3C/Fe^0 system as compared to chloramphenicol

Nan Zhao[a], Kunyuan Liu[a], Chao He[a], Jia Gao[a], Weihua Zhang[a,*], Tingjie Zhao[a], Daniel C.W. Tsang[b], Rongliang Qiu[a,c,*]

[a] School of Environmental Science and Engineering, Guangdong Provincial Key Lab of Environmental Pollution Control and Remediation Technology, Sun Yat-sen University, Guangzhou 510006, PR China
[b] Department of Civil and Environmental Engineering, The Hong Kong Polytechnic University, Hung Hom, Kowloon, Hong Kong, China
[c] Guangdong Laboratory for Lingnan Modern Agriculture, College of Natural Resources and Environment, South China Agricultural University, Guangzhou 510642, PR China

ARTICLE INFO

Keywords:
C/Fe_3C/Fe^0 composite
Fe^0
Biochar
Antibiotics adsorption
Oxidative degradation
Stability/reusability

ABSTRACT

Reactive oxygen species (ROS) production for Fe^0 is limited because of the formed iron corrosion products. In this study, C/Fe_3C/Fe^0 composite which produces enhanced ROS has been specifically designed and fabricated to remove typical antibiotics (i.e., oxytetracycline (OTC) and chloramphenicol (CAP)) as a heterogeneous Fenton-like catalyst. The C/Fe_3C/Fe^0 composite demonstrated excellent performance for both OTC and CAP removal as compared with Fe^0 and biochar. Furthermore, X-ray photoelectron spectrometry, Fourier transform infrared spectrometry, high performance liquid chromatography-mass spectra and electron spin resonance analyses were conducted to elucidate the adsorption and degradation mechanisms. The adsorption of OTC and CAP was mainly dominated by H bonds and the electron-acceptor-acceptor on the surface of the C/Fe_3C/Fe^0 composite, respectively. In particular, $^{\cdot}OH$ simultaneously induced the degradation of OTC and CAP, while $^1O_2$ presented the selective oxidation to OTC. More specifically, the degradation of OTC over C/Fe_3C/Fe^0 was stronger and faster than that of CAP, leading to 65.84% and 16.84% of removal efficiency for OTC and CAP, respectively. Furthermore, C/Fe_3C/Fe^0 exhibited superior reusability and stability after regeneration, but regenerated Fe^0 almost lost its reactivity. Therefore, the efficiency in situ generation of $^1O_2$ using C/Fe_3C/Fe^0 would shed new light on the selective oxidation of aqueous organic compounds.

1. Introduction

Antibiotics are very important to human life. However, they have attracted a growing concern due to their toxicity to the aquatic ecosystem and the development of antibiotic resistant bacteria (Kemper, 2008; Szymanska et al., 2019), which increasingly threaten human health (Li et al., 2019a). Among antibiotics, oxytetracycline (OTC) and chloramphenicol (CAP) are broad-spectrum antibiotics that have been widely used to treat bacterial infections. CAP is more hydrophobic than OTC. These two antibiotics have been detected in drinking water, surface water and groundwater (Jiang et al., 2011; Kolpin et al., 2002; Lindsey et al., 2001) and posed serious risk to the environment. Previous studies have shown that OTC and CAP are difficult to be biodegraded and they were more persistent than other contaminants in the environments (Chen et al., 2016; Wang and Yates, 2008). Therefore, their biodegradation often occurs at a very low rate (Chen et al., 2019; Navada and Kulal, 2019). Thus, adsorption and chemical degradation methods are attractive approaches to eliminate them. To date, the composites of biochar with nano-scale Fe^0 and their application are widely studied (Ahmed et al., 2017b; Wu et al., 2018; Xu et al., 2020; Zhu et al., 2019).

Biochar (BC) is a kind of low-cost adsorbent with many surface functional groups, but its adsorption capacity is often restricted by its limited surface area, and its degradation ability is very weak (Mao et al., 2019). Nano-scale Fe^0 has become a study hot topic thanks to its high reactivity for the degradation of many antibiotics, and its oxidation product Fe(III) was reported to chelate with some antibiotics (Bi et al., 2016). Nano-scale Fe^0 can degrade organic contaminant by reduction (Lei et al., 2018a; Zhao et al., 2019). It can also activate molecular oxygen to produce reactive oxygen species (ROS) such as $^{\cdot}OH$

* Corresponding authors at: School of Environmental Science and Engineering, Guangdong Provincial Key Lab of Environmental Pollution Control and Remediation Technology, Sun Yat-sen University, Guangzhou 510006, PR China (R. Qiu).
E-mail addresses: zhangwh5@mail.sysu.edu.cn (W. Zhang), eesqrl@mail.sysu.edu.cn (R. Qiu).

https://doi.org/10.1016/j.envint.2020.105899
Received 22 February 2020; Received in revised form 16 May 2020; Accepted 13 June 2020

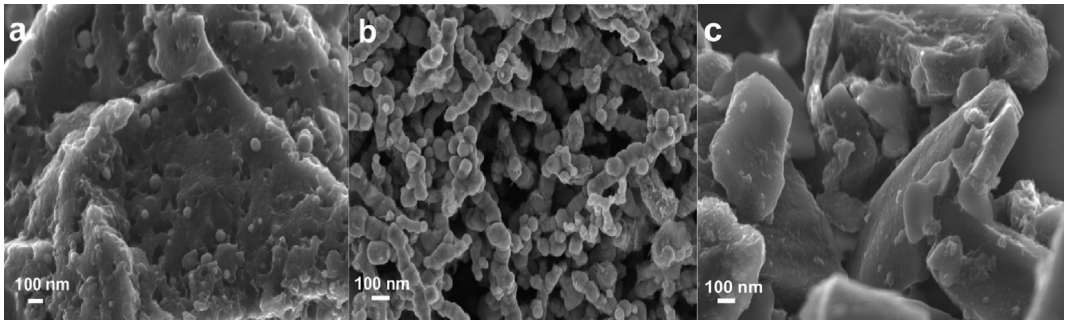

Fig. 1. SEM spectra of (a) C/Fe_3C/Fe^0, (b) Fe^0 and (c) biochar.

for the degradation of organic contaminants (Shen et al., 2018). However, nano-scale Fe^0 is easily oxidized and releases into water, reducing the yield of ROS (Erdim et al., 2015; Lei et al., 2018b). Therefore, its utilization is greatly limited.

To enhance the adsorption capacities of biochar and increase the production ability of ROS for the nano-scale Fe^0, nano-Fe^0 has been loaded on biochar to obtain the stable C/Fe composites with both adsorption and degradation capacities (Ahmed et al., 2017b; Li et al., 2019b; Mao et al., 2019; Sun et al., 2019). The C═C aromatic carbon along with −OH groups in biochar could adsorb CAP by a stronger electron-donor-acceptor interaction (Ahmed et al., 2017a). OTC can also form complexation with −COOH groups (Luo et al., 2018). The BC/Fe^0/H_2O_2 system has been shown to enhance the activation of H_2O_2 to generate more $^{\cdot}OH$ for the degradation of ciprofloxacin than sole BC or Fe^0 (Mao et al., 2019). In the Fe/CB600/PMS system, $O_2^{\cdot -}$ and $^1O_2$ were validated as the predominant ROS for the removal of trichloroethylene (Li et al., 2020).

Until now, few papers have reported the production of ROS in C/Fe composite without the addition of any oxidants. The relative contribution of adsorption and degradation has not been fully understood. Some research studies just focused on the degradation, while some only paid attention to the adsorption behavior (Hsu et al., 2018; Misra et al., 2018; Wang et al., 2015). Therefore, fully understanding the underlying adsorption and degradation mechanisms of these antibiotics on the surface of C/Fe_3C/Fe^0 composite is critical for the design of the C/Fe material and optimization of operational conditions to achieve high removal efficiency.

It is still not very clear what kind of ROS will be produced when the C/Fe_3C/Fe^0 composite contacts with antibiotics such as OTC and CAP? Moreover, what are the specific structures and properties of organics that relate with the removal behaviors? To answer these questions, the C/Fe_3C/Fe^0 composite, nano-scale Fe^0 and biochar as the corresponding benchmarks were synthesized and used for the removal of OTC and CAP. Detailed mechanisms of the adsorption and degradation were investigated by X-ray photoelectron spectrometry (XPS), Fourier transform infrared spectra (FTIR), high-performance liquid chromatography-mass spectrometry (HPLC-MS) and electron spin resonance (ESR) analysis. Furthermore, the quantitative contribution of adsorption and degradation to the removal of OTC and CAP was calculated. The findings of this study will be beneficial for promoting the potential application of C/Fe_3C/Fe^0 composites to remove antibiotics.

2. Materials and methods

2.1. Preparation of C/Fe_3C/Fe^0, Fe^0, and biochar

C/Fe_3C/Fe^0 composite was produced by mixing 400 mg of 300 °C corn stalk biochar with $Fe(NO_3)_3{\cdot}9H_2O$ (1000 mg) in 50 mL of ultrapure water. The used high content of Fe was beneficial for the formation of graphite. After stirring at room temperature for 7 h, the mixture was dried at 105 °C for 48 h. At last, the dried mixture was transferred to a tube furnace and pyrolyzed at 800 °C for 2 h under a N_2 atmosphere. Fe^0 was obtained by adding excessive $NaBH_4$ solution dropwise into 50 mL of 20 g/L $FeSO_4$ solution and stirring for 2 h to reduce Fe(II) to Fe^0 under a N_2 atmosphere. The produced Fe^0 was collected by filtration, washed with ethanol and dried in an oven at 105 °C. The biochar studied herein as the benchmark was prepared by pyrolyzing the above-mentioned corn stalk biochar in the tube furnace at 800 °C for 2 h under a N_2 atmosphere.

2.2. Experiments for antibiotic removal

The dynamic experiments of OTC or CAP removal were conducted by mixing 0.0120 g of the C/Fe_3C/Fe^0 composite, Fe^0 or biochar samples with 15 mL of 0.1 mM OTC or CAP solution on a 180 rpm shaker at 25 ± 1 °C for different periods of time (0–24 h) under aerobic condition. Then, the mixtures were centrifuged at 3000 rpm for 5 min, and the supernatant was filtered through a 0.22 μm membrane for the residual OTC and CAP concentration determination with a UV–vis spectroscopy at 272 nm and 277 nm (Jo et al. 2017; Liu et al. 2019; Xu et al. 2018; Yao et al., 2019). Moreover, the control experiment with the biochar and ultrapure water without OTC or CAP was also conducted to exclude the interference of biochar impurity or natural organic matter on the UV analyses.

The static OTC or CAP removal under different initial concentrations was also investigated by agitating 0.0120 g of the C/Fe_3C/Fe^0 composite, Fe^0 or biochar samples in 15 mL of 0.1–0.7 mM OTC or 0.01–1.5 mM CAP solutions for 24 h. The detailed procedures were similar to the dynamic experiments. All experiments were duplicated, and the average and standard deviation were recorded.

3. Results and discussion

3.1. Characterization of C/Fe_3C/Fe^0, Fe^0 and biochar

The SEM and TEM spectra of C/Fe_3C/Fe^0 (a), Fe^0 (b) and biochar (c) with their surface morphologies are presented in Figs. 1 and 2. As illustrated in Fig. 1a, spherical iron crystal particles were attached on or entered into the porous surface of biochar in C/Fe_3C/Fe^0. According to Fig. 2a, the sizes of iron nanoparticles were in the range of 17–61 nm. In addition, carbon shells formed owing to the interactions between carbon atoms and iron (Efimov et al., 2018). These carbon shells were well recognizable around larger iron nanoparticles. On the images of Fe^0 (Figs. 1b and 2b), the iron nanoscale particles were clustered with each other in chains due to magnetic and electronic interactions (Xiao et al., 2014) and gradually aggregated into larger ones. Fig. 1c displays that biochar had flaky structure, and no porous structures were observed which might be destroyed under very high temperature (800 °C). For biochar, the carbon fraction is primarily in the amorphous form.

The N_2 adsorption-desorption isotherms of these three materials are shown in Fig. S1, and the textural properties are presented in Table S1. The N_2 adsorption/desorption of C/Fe_3C/Fe^0 and Fe^0 presented typical

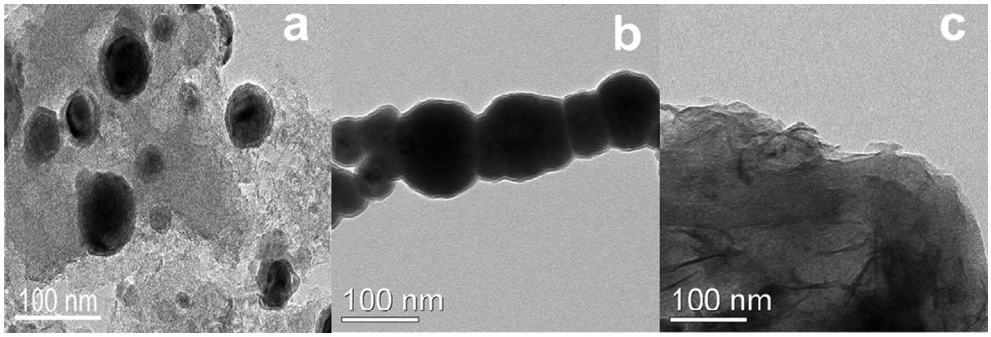

Fig. 2. TEM images of (a) C/Fe_3C/Fe^0, (b) Fe^0 and (c) biochar.

type IV isotherm according to IUPAC classification with abundant mesoporosity, while biochar showed very little N_2 adsorption capacity, which implied that it was almost non-porous (Tiwari et al., 2018). This might because that high temperature destroyed the porous structures of biochar. As listed in Table S1, the surface areas of C/Fe_3C/Fe^0 and Fe^0 were 116.86 and 23.60 m^2/g with the mesopore volume of 0.090 and 0.076 cm^3/g, respectively, and their mesopore ratios were 75.63% and 65.79%. C/Fe_3C/Fe^0 exhibited improved textural properties as compared to biochar. Inhomogeneous nanoparticles in C/Fe_3C/Fe^0 composite always led to a porous and loose structure (Zeng et al., 2018), increasing its surface area. Moreover, the produced CO_2, CO and H_2 (Yan et al., 2013) by the reduction of Fe^{3+}/Fe^{2+} to Fe^0 also benefited the pore formation. Therefore, the surface area of biochar was much lower than that of C/Fe_3C/Fe^0.

The XRD patterns exhibited the well-defined crystalline C/Fe_3C/Fe^0, as assigned in Fig. S2, and a small peak at 25.96° confirmed its highly graphitic layered carbon structure (Liu et al., 2016). Its prominent peaks at 37.75°, 42.89°, 43.75°, 44.57°, 44.99°, 45.87°, 51.83°, 54.41° and 74.51°, corresponding to the (2 1 0), (2 1 1), (1 0 2), (2 2 0), (0 3 1), (1 1 2), (1 2 2), (0 4 0) and (4 0 0) diffraction lattice faces, respectively, were in good agreement with the standard diffraction pattern of Fe_3C. Thus, the XRD results indicated that iron was successfully immobilized onto biochar. The diffraction peaks at 44.67°, 65.02° and 82.32° were observed in the XRD patterns of both C/Fe_3C/Fe^0 composite and pure Fe^0 prepared by the reduction of $NaBH_4$ (Figs. S2a and S2b). They could be indexed to the (1 1 0), (2 0 0) and (2 1 1) planes of Fe^0, revealing that there was Fe^0 in the C/Fe_3C/Fe^0 composites. The peaks at 20.83°, 26.61°, 36.49°, 39.43°, 40.24°, 50.08°, 54.80°, 59.86°, 68.06°, and 68.20° confirmed that SiO_2 existed in the biochar.

The XPS spectra in Fig. S3 indicate that the surface of C/Fe_3C/Fe^0 was enriched with C and O, while Fe was not detected. It confirms the existence of a carbon shell on the cover of C/Fe_3C/Fe^0 composites, with a greater C atomic percentage (75.09%) than biochar (67.61%). On the surface of Fe^0, three prominent peaks corresponding to C_{1s}, O_{1s} and Fe_{2p} were detected. The peaks attributing to C_{1s}, O_{1s}, N_{1s}, Si_{2p} and K_{2p} were observed on the surface of biochar.

3.2. Removal of antibiotics

The kinetic removal performances of C/Fe_3C/Fe^0, Fe^0 and biochar for OTC and CAP are presented in Fig. 3. Obviously, biochar had the lowest removal capacity for these antibiotics with the slowest removal rate. Both antibiotics removal initially soared within a short period and later levelled off at 480 min for C/Fe_3C/Fe^0 and Fe^0. The kinetic data were fitted with pseudo first-order and second-order kinetic models, and the corresponding parameters are summarized in Table S2. The rate constant k_2 (1.477 g/(g·min)) of OTC removal by C/Fe_3C/Fe^0 was double of that by Fe^0 (0.708 g/(g·min)). Although the removal of CAP seems to be faster by Fe^0 than C/Fe_3C/Fe^0, the residual amounts of CAP in the solution after treating with C/Fe_3C/Fe^0 were lower than that with Fe^0. Pseudo second-order kinetic model was found to fit quite well

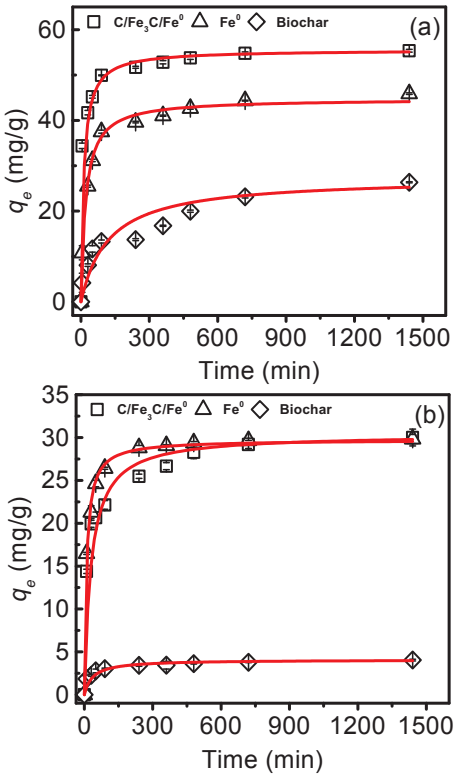

Fig. 3. The dynamic removal of (a) OTC and (b) CAP. Lines represent Pseudo second-order kinetic fitting and the bars are standard deviation.

(R^2 > 0.973), indicating that the removal process mainly depended on chemical interactions (Zhao et al., 2017a).

Fig. S4 presents the increasing removal of OTC and CAP with the initial concentrations. C/Fe_3C/Fe^0 composite was found to remove as high as 167.73 mg/g OTC, much higher than Fe^0, biochar and many reported adsorbents (Table S3). Similarly, C/Fe_3C/Fe^0 composite could remove slightly greater amounts of CAP than Fe^0, and 5.14 times that of biochar. These results confirmed that C/Fe_3C/Fe^0 owned a greater capacity to remove antibiotics compared with Fe^0 and biochar. Meanwhile, when the initial concentration of OTC and CAP was 0.5 mM, the removal amounts of OTC on three materials were 137.11 mg/g, 112.45 mg/g and 92.70 mg/g, respectively, which were higher than those of CAP. Hydrophilic compounds were recalcitrant to be adsorbed in the solid. As a result, degradation might be the dominant removal mechanism which gave rise to higher removal amounts of OTC than CAP.

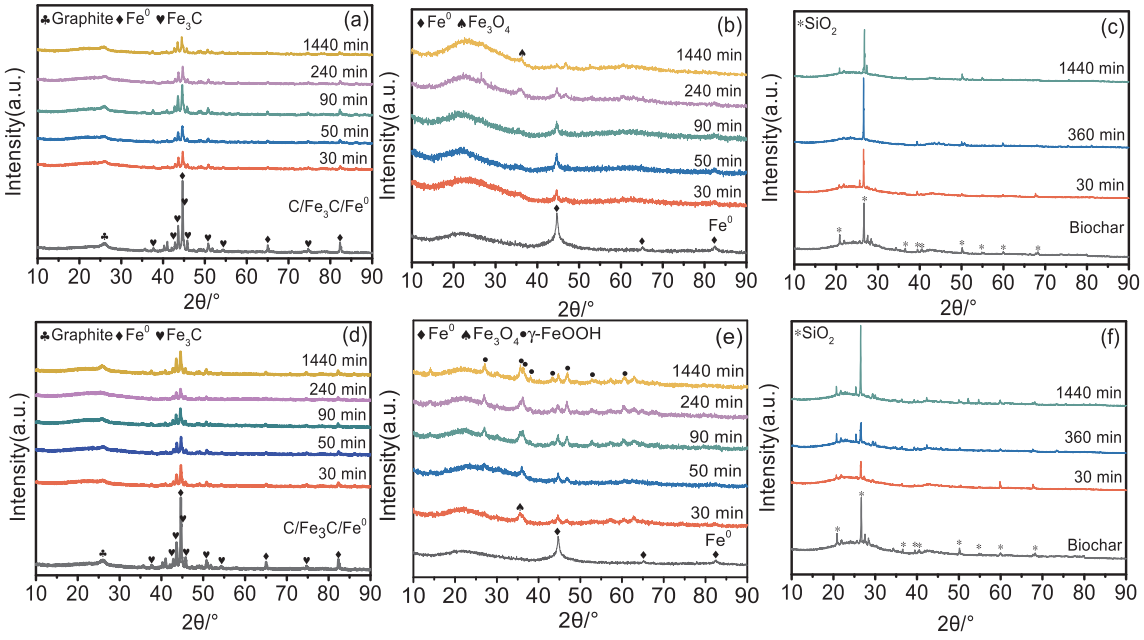

Fig. 4. (a), (b), (c) XRD patterns of materials after reacting with OTC; (d), (e), (f) XRD patterns of materials after reacting with CAP at different time.

3.3. Corrosion resistance of the materials

It was important to consider the corrosion resistance of the materials regarding to their potential application in wastewater treatment. The XRD patterns of $C/Fe_3C/Fe^0$, Fe^0 and biochar after the reactions with antibiotics are shown in Fig. 4. No change occurred during the removal process of antibiotics by biochar. However, the peak intensity at $2\theta = 44.67°$ dramatically decreased for $C/Fe_3C/Fe^0$ and Fe^0, suggesting that iron was involved in the reaction, which might form a complex with antibiotics (Bi et al., 2016). During the reaction process, $C/Fe_3C/Fe^0$ kept its state, and no iron oxide ($2\theta = 35.39°$) was formed, indicating that $C/Fe_3C/Fe^0$ displayed a good stability with the cover of graphite. Fe^0 became iron oxide after reacting with OTC and CAP at 240 min and 30 min, respectively. For the removal of CAP, the oxidation of Fe^0 happened very fast, and γ-FeOOH ($2\theta = 27.04°$, as illustrated in Fig. 4e) was formed at 90 min, which corresponded to water adsorption and corrosion (Vollprecht et al., 2019). This process decreased the electron transfer rate and ROS yield (Erdim et al., 2015). Meanwhile, the formation of a passive layer enhanced the precipitation and surface area (67.81 m^2/g). Therefore, Fe^0 removed CAP faster than $C/Fe_3C/Fe^0$. From the above analysis, the iron corrosion was written as:

$$Fe^0 + 2H_2O \rightarrow Fe^{2+} + H_2 + 2OH^- \quad (1)$$

$$2Fe^0 + O_2 + 2H_2O \rightarrow 2Fe^{2+} + 4OH^- \quad (2)$$

$$6Fe^{2+} + O_2 + 6H_2O \rightarrow 2Fe_3O_4 + 12H^+ \quad (3)$$

$$4Fe^{2+} + O_2 + 6H_2O \rightarrow 4FeOOH + 8H^+ \quad (4)$$

The corrosion of iron was accompanied by the release of iron. Therefore, the iron dissolution from $C/Fe_3C/Fe^0$ and Fe^0 was continuously observed along the removal process. The amounts of iron dissolved in the OTC solution for Fe^0 were much higher than that of $C/Fe_3C/Fe^0$. The very quick increase in concentrations of total iron in the OTC solution was observed during the first 30 min (Fig. S5a). After the slowdown, the iron elution reached equilibrium at 240 min with the concentration of total Fe ion up to 5.61 mg/L. Iron oxide formed at 240 min, as confirmed by XRD spectra illustrated in Fig. 4b, led to a large amount of iron eluted into the solution. The adsorption and precipitation were inhibited, which led to a slower removal rate as compared to $C/Fe_3C/Fe^0$. By contrast, for the CAP solution, the maximum iron elution concentration was only 42.30 μg/L for Fe^0, because the passive iron oxide or γ-FeOOH, confirmed by XRD spectra in Fig. 4e, covered the entire surface of Fe^0, therefore blocking the further iron elution (Harada et al., 2016). Interestingly, the total Fe ion concentrations in the OTC and CAP solutions were close to zero for $C/Fe_3C/Fe^0$, which clearly exhibited a good stability with much reduced secondary pollution caused by iron elution.

We also investigated the Fe 2p3/2 spectra of $C/Fe_3C/Fe^0$ and Fe^0 after the reaction with antibiotics at 24 h to further understand the stability of materials (Fig. 5). Peaks A and B were due to Fe^0 while the other peaks were assigned to Fe(II) and Fe(III) in iron oxides (Grosvenor et al., 2004; Yang et al., 2019; Zhao et al., 2018). The Fe^0 contents were 13.67% and 6.58% on the surface of $C/Fe_3C/Fe^0$ after the reaction, which were higher than those of Fe^0 (0.37% and 1.31%). This further demonstrated that $C/Fe_3C/Fe^0$ was more stable and iron corrosion was inhibited.

3.4. Adsorption mechanisms

To further understand the adsorption mechanisms of antibiotics on $C/Fe_3C/Fe^0$ and Fe^0, we investigated the XPS and FTIR spectra after the reaction of OTC and CAP (Figs. 6 and S8). Some new peaks at 398.88 (N 1s) appeared after the reaction as compared to the XPS spectra in Figs. S3a and 3b. The increased content of N indicated that N containing groups in OTC and CAP were adsorbed on the surface of $C/Fe_3C/Fe^0$ and Fe^0. Simultaneously, the peak at Fe 2p also appeared for the $C/Fe_3C/Fe^0$ sample, which suggested that iron was exposed to the surface after 24 h of reaction. As shown in Fig. 6 of the FTIR spectra, the bands ranging from 3419 to 3422 cm^{-1} in $C/Fe_3C/Fe^0$ and Fe^0 were assigned to bulk OH (Park et al., 2019). After the reaction of OTC with $C/Fe_3C/Fe^0$ and Fe^0, the bands at 3422 cm^{-1} and 3419 cm^{-1} shifted to the lower frequency 3415 cm^{-1} and 3405 cm^{-1}, respectively. These changes indicated that H bonds were formed (Zhao et al., 2017a). The ability of OTC to form H bonds with $C/Fe_3C/Fe^0$ and Fe^0 was higher than that of CAP, as evidenced by more OH groups in OTC molecules (Liao et al., 2013). No H bonds formed in the reaction of CAP with the $C/Fe_3C/Fe^0$ composite, but the peak intensity of 3415 cm^{-1} in $C/Fe_3C/Fe^0$ shortened, indicating that the involvement of carboxyl group led to the breakage of OH bonds (Devi and Saroha, 2015). In addition, an electron-acceptor-acceptor interaction might occur for the carboxyl

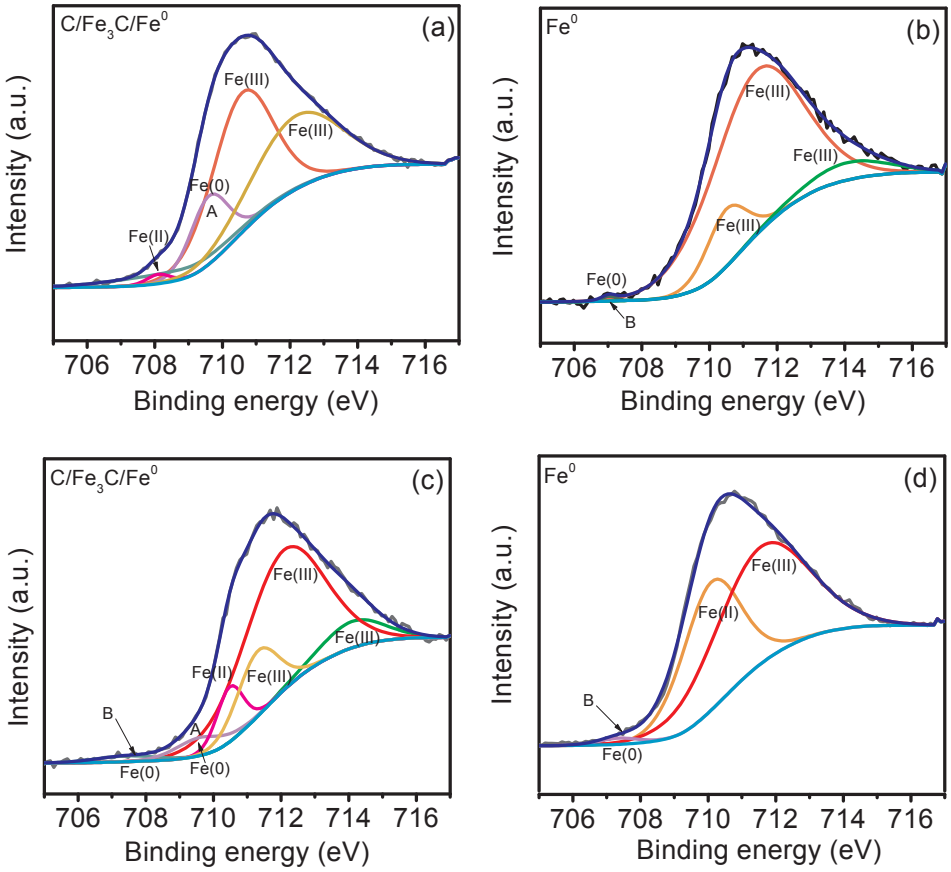

Fig. 5. (a), (b) XPS analysis of Fe 2p3/2 spectrum for used materials after reacting with OTC; (c), (d) XPS analysis of Fe 2p3/2 spectrum for used materials after reacting with CAP Fe^0 at 24 h.

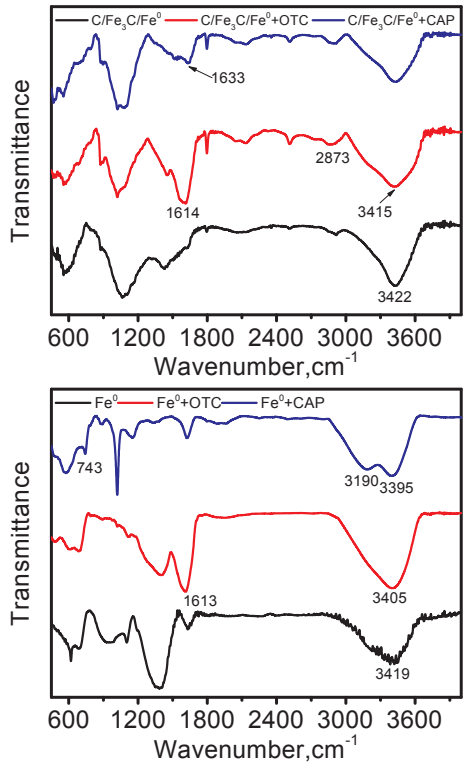

Fig. 6. FTIR spectra of $C/Fe_3C/Fe^0$ composite and Fe^0 before and after the reaction of OTC and CAP.

group in the $C/Fe_3C/Fe^0$ composite and nitro groups in its arene units of CAP. A similar result was also reported by Ahmed et al. (2017b). The appearance of two strong peaks at 3395 and 3190 cm^{-1} suggested that the amide groups of CAP were adsorbed by Fe^0 (Oliveira et al., 2019). The band at 2873 cm^{-1} was attributed to the stretching vibration of the CH_3 groups (Chen et al., 2011). The appearance of this new band was the consequence of the interaction between methyl groups of OTC and $C/Fe_3C/Fe^0$ (Zhao et al., 2017b). The band at 1730 cm^{-1} was indicative of C=O stretching vibration. The intensity of this band greatly increased after the adsorption of OTC and CAP by $C/Fe_3C/Fe^0$, which indicated that C=O in the OTC and CAP molecules were adsorbed (Fernandes et al., 2019). Simultaneously, the bands at 1614 and 1633 cm^{-1} appeared, possibly due to the adsorption of aromatic skeletal C=C vibration in OTC and CAP by $C/Fe_3C/Fe^0$. This phenomenon also occurred for the removal of OTC by Fe^0. The presence of aromatic C-H bend (out of the plane) groups at 743 cm^{-1} in the Fe^0 + CAP sample confirmed that the aromatic C-H groups of CAP were adsorbed by Fe^0.

3.5. Degradation products and degradation pathways

Fig. S9 displays the ion chromatograms of OTC after the reaction with $C/Fe_3C/Fe^0$ and Fe^0 at different contact times. The appearance of small peaks of A (*m/z* 357, 7.91 min Retention Time (RT)) at 10 s confirmed a fast degradation process. At 30 min, the initial OTC peak (*m/z* 461, 3.24 min RT) disappeared after the reaction with $C/Fe_3C/Fe^0$, revealing a more efficient OTC removal by $C/Fe_3C/Fe^0$ than Fe^0. Comparatively, the removal rate of CAP on $C/Fe_3C/Fe^0$ was slower. Only a very small amount of degradation product C (*m/z* 127, 1.65 min RT) was detected at 10 min in CAP solution with $C/Fe_3C/Fe^0$. Most of the macromolecular CAP existed in the solution and was not adsorbed

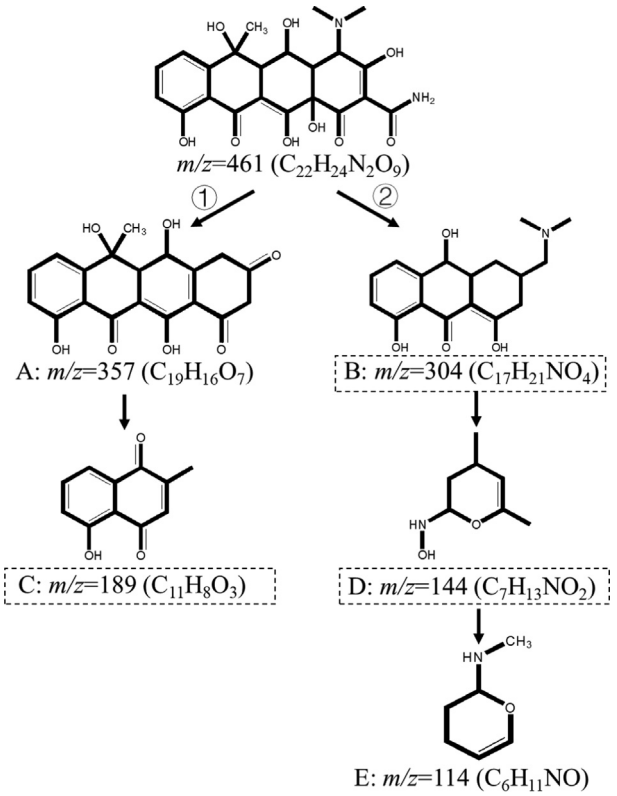

Fig. 7. Proposed degradation pathway of OTC by C/Fe_3C/Fe^0 composite and Fe^0. Dotted square means the product was not detected in the solution, which might be adsorbed on the surface of C/Fe_3C/Fe^0 composite.

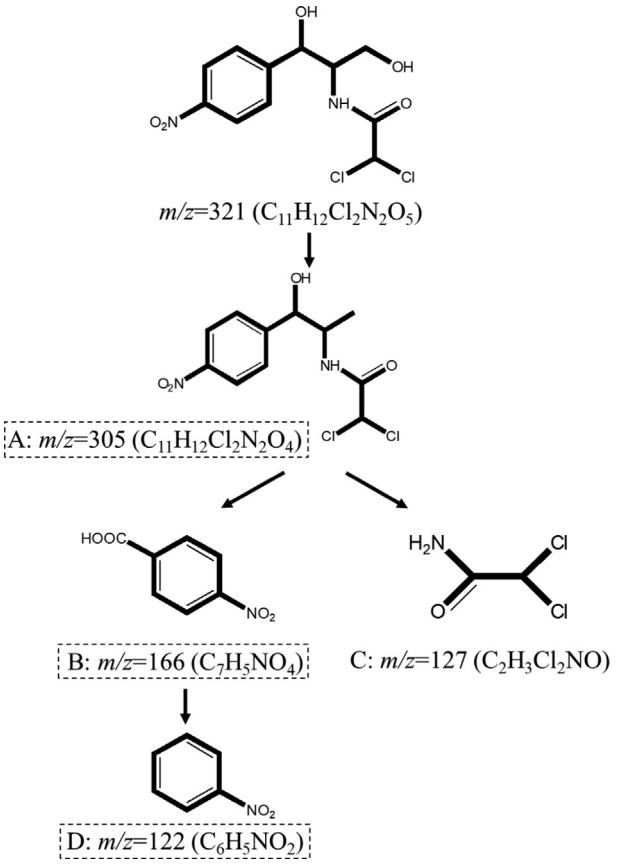

Fig. 8. Proposed degradation pathway of CAP by C/Fe_3C/Fe^0 composite and Fe^0. Dotted square means the product was not detected in the solution, which might be adsorbed on the surface of C/Fe_3C/Fe^0 composite.

or degraded at 24 h. This accounted for a lower removal amount of CAP on C/Fe_3C/Fe^0 compared to OTC. The peak intensity of dichloroacetamide (C) increased with reaction time in Fig. S10f, which might lead to higher UV intensity and lower TOC removal efficiency at 24 h (Figs. S6 and S7b). The smaller amounts of degradation products in C/Fe_3C/Fe^0 system than that of Fe^0 implied that C/Fe_3C/Fe^0 was ineffective to directly degrade OTC and CAP into the solution, and more degradation might occur on the surface of C/Fe_3C/Fe^0.

According to the HPLC-MS results, the main degradation products of OTC and CAP by C/Fe_3C/Fe^0 and Fe^0 were exhibited in Figs. 7 and 8. In Fig. 7, the possible degradation pathways of OTC contained two routes. For route 1, the hydrogen abstraction and the loss of hydroxyls, amide and N, N-dimethyl groups possibly accounted for the production of A. Then, the further oxidation led to the opening of aromatic ring to form 5-hydroxy-2-methylnaphthalene-1,4-dione. In route 2, product B was stemmed from dehydroxylation, demethylation, deamidation and opening of the aromatic ring, and then gradually oxidized to product D. Finally, product D underwent demethylation and dehydroxylation to form N-methyl-3,4-dihydro-2H-pyran-2-amine.

In Fig. 8, peak A was mainly in 305 (*m/z*), suggesting that the chlorine in molecular had not been lost yet. The drop in 16 (*m/z*) resulting from the loss of O was due to the low bond energy of C-O (Wu et al., 2018). It was postulated that product A was further degraded to two products (*p*-nitrobenzoic acid and dichloroacetamide). At last, nitrobenzene was formed by decarboxylation. The previous study has shown that CAP could be degraded by nano zerovalent iron through the reduction reaction (Ahmed et al., 2017b). However, no reduction product was detected in this study. Thus, the degradation of CAP on Fe^0 was dominated by oxidation.

3.6. Quantification of adsorption and degradation

To confirm the degradation mechanism, electron spin resonance spectra were used to determine the generation of ROS. In Fig. S11a, we found the four characteristic lines with the intensity ratio of 1:2:2:1 ascribed to the signal of $^{\cdot}OH$ for both C/Fe_3C/Fe^0 and Fe^0 systems. The noticeable 1:1:1 three-line patterns attributed to the formation of TEMP-$^1O_2$ adducts were observed in Fig. S11b. These results demonstrated that $^{\cdot}OH$ and $^1O_2$ were generated. Graphite is a conductor and iron oxide is a semiconductor. They could directly transmit electron from the inner iron core to the adsorbed oxygen, and activate O_2 to generate $^{\cdot}OH$ through Fenton reaction (Eqs. (5) and (6); Guan et al., 2015). The Fe^{2+} species could react with dissolved oxygen through electron transfer forming $O_2^{\cdot -}$ (Eqs. 7; Yang et al., 2019). Then, the recombination of $O_2^{\cdot -}$ led to the production $^1O_2$ (Eqs. 8). The inference was also proved by several experimental results by non-photochemical methods or without the addition of oxidants (Bokare and Choi, 2015; Rayaroth et al., 2019). Meanwhile, our experiment with N_2 bubbling to remove dissolved oxygen in solution, as illustrated in Fig. S12, showed that the decrease for the removal efficiency of OTC by C/Fe_3C/Fe^0 and Fe^0 was observed with the increasing time of N_2 bubbling. This indicated that the decrease of O_2 led to the reduction of $O_2^{\cdot -}$ and $^1O_2$ and indirectly consolidated that $^1O_2$ can be derived from the recombination of $O_2^{\cdot -}$.

$$Fe^0 + O_2 + 2H^+ \rightarrow Fe^{2+} + H_2O_2 \quad (5)$$

$$Fe^0 + H_2O_2 \rightarrow Fe^{2+} + {}^{\cdot}OH + OH^- \quad (6)$$

$$Fe^{2+} + O_2 \rightarrow O_2^{\cdot -} + Fe^{3+} \quad (7)$$

$$O_2^{\cdot -} + O_2^{\cdot -} + 2H^+ \rightarrow {}^1O_2 + H_2O_2 \quad (8)$$

The signals of $^{\cdot}OH$ and $^1O_2$ in the C/Fe_3C/Fe^0 system were much stronger than that of Fe^0 system, indicating that more $^{\cdot}OH$ and $^1O_2$

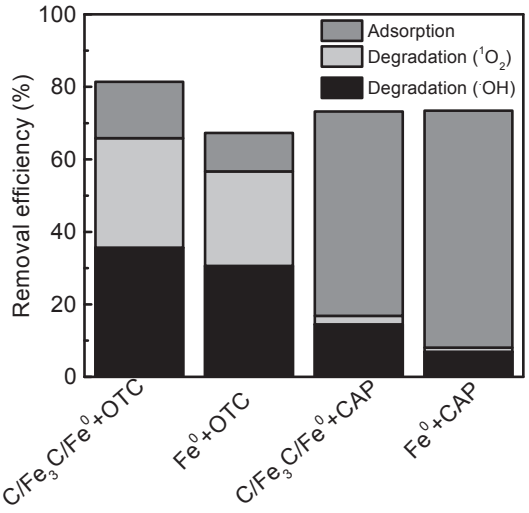

Fig. 9. Quantitative removal of OTC and CAP on $C/Fe_3C/Fe^0$ composite and Fe^0 by adsorption and degradation at 24 h.

were generated in the $C/Fe_3C/Fe^0$ system. Hence, the $C/Fe_3C/Fe^0$ composite owned a superior molecular oxygen activation performance over Fe^0. In the $C/Fe_3C/Fe^0$ composite, the Fe content was only 24.60%, which was much lower than that of Fe^0. Meanwhile, biochar has a weak activation ability (Mao et al., 2019), but biochar could promote $C/Fe_3C/Fe^0$ in the activation of O_2 because most $C/Fe_3C/Fe^0$ particles were uniformly distributed on the biochar surface, which avoided the agglomeration of nanoparticles. Moreover, the middle layer of Fe_3C efficiently catalyzed electron transfer from the core Fe^0 to the external graphite surface.

Quenching tests were conducted to confirm the effects of $^{\cdot}OH$ and $^1O_2$ on the OTC and CAP degradation in the $C/Fe_3C/Fe^0$ and Fe^0 systems. Tert butyl alcohol (TBA) and NaN_3 were used as the scavengers for $^{\cdot}OH$ and $^1O_2$, respectively. The results showed that the OTC removal efficiency decreased from 81.38% to 45.73% and 51.19% with the addition of 0.1 M TBA and 1 mM NaN_3, respectively (Fig. S13). Hence, the removal efficiencies of 35.65% and 30.19% were attributed to the degradation (Fig. 9). For Fe^0, 30.63% and 26.06% were caused by the degradation through $^{\cdot}OH$ and $^1O_2$, respectively.

In the removal process of CAP by $C/Fe_3C/Fe^0$ and Fe^0, oxidation occurred quickly and hindered the electron transfer between Fe^0 and the adsorbed oxygen. Therefore, the degradation efficiencies only accounted for 16.84% and 8.08%. The degradation efficiency of $C/Fe_3C/Fe^0$ was 2 times that of Fe^0 due to the higher signal intensity of ROS. $^{\cdot}OH$ was the main ROS responsible for the CAP degradation and $^1O_2$ had little effect. Previous studies have shown that $^{\cdot}OH$ and $O_2^{\cdot -}$ played important roles in the degradation of organic contaminants by Fe^0-based materials (Harada et al., 2016, Shen et al., 2018, Yang et al., 2019). $^1O_2$ was seldom found in the removal of organic contaminants by non-photochemical methods or without the addition of oxidants. In our studies, $^1O_2$ was produced by the initially-formed $O_2^{\cdot -}$ and showed a higher selective reactivity toward OTC in $C/Fe_3C/Fe^0$ system.

From the above analysis, we inferred that the OTC removed by $C/Fe_3C/Fe^0$ and Fe^0 involved two steps: (1) Small parts of OTC molecules and the degradation intermediates were adsorbed onto the surface by H bonding; (2) $^{\cdot}OH$ and $^1O_2$ were produced to degrade most OTC molecules by oxidation. CAP presented a different phenomenon due to the distinct physical-chemical properties of the two antibiotics. The log K_{ow} value of OTC was much smaller than that of CAP, indicating the greater hydrophobicity of CAP (Table S4). The hydrophobic effect had a minor contribution to antibiotics adsorption (Liao et al., 2013). The greater number of H-bond acceptor/donors in OTC molecule than in CAP confirmed that OTC is easier to form hydrogen bonds, which drove the OTC to be adsorbed on $C/Fe_3C/Fe^0$ composite. Thus, H bonds made the fast contact of OTC with the materials. Most CAP molecules and the degradation intermediates were slowly adsorbed on the $C/Fe_3C/Fe^0$ composite due to the weak interaction. Water molecules were preferentially adsorbed by $C/Fe_3C/Fe^0$ composite and Fe^0, which led to the quick oxidation and formation of iron oxide. Oxidized Fe^0 had lower degradation and mineralization capacities for the degradation products due to the increased amounts of dichloroacetamide and decreased TOC removal efficiency, which would cause the secondary pollution.

3.7. Reusability of materials

Recycle experiments were performed to evaluate the reusability of $C/Fe_3C/Fe^0$ and Fe^0 on the removal of OTC and CAP. As shown in Fig. S14, the removal efficiency of OTC on $C/Fe_3C/Fe^0$ increased from 81.38% to 84.15% after the second cycle. Because high temperature desorption reactivated the $C/Fe_3C/Fe^0$ composite, thus the removal efficiency was enhanced. Even in the fourth time, the removal efficiency of OTC on $C/Fe_3C/Fe^0$ was 77.08%. But for Fe^0, the removal efficiency gradually dropped from 67.29% to 23.05%. The XRD patterns displayed that iron oxide appeared after the first usage, and γ-FeOOH occurred after the second cycle (Fig. S15b). The $C/Fe_3C/Fe^0$ composite kept its original state until the fourth usage and only a small peak of iron oxide appeared after the third cycle. Furthermore, the peaks at 44.67° showed higher intensity after second, third and fourth usage, which indicated that high temperature desorption could increase the Fe^0 crystallinity.

For the removal of CAP on Fe^0, the removal efficiency dropped sharply from 72.78% to 2.7% after the second cycle. No absorption peak of acetamide was produced (Fig. S16d) and Fe^0 could only be used once to remove CAP. The formation of γ-FeOOH made it totally lose the removal capacity (Fig. S15d). In the $C/Fe_3C/Fe^0$ composite, the iron oxide was formed after the second cycle. Oxidation was stronger than the system of $C/Fe_3C/Fe^0$ with OTC. Compared with the reuse capacity of Fe^0, the removal efficiency of CAP on $C/Fe_3C/Fe^0$ was only reduced by 6.87% after four times of usage. Thus, $C/Fe_3C/Fe^0$ had a much better reusability and presented a great application superiority.

4. Conclusions

Due to enhanced formation of ROS, $C/Fe_3C/Fe^0$ displayed a superior performance in removing OTC and CAP. This composite could prevent organic contaminants from being released back to the solution. OTC and CAP were adsorbed by $C/Fe_3C/Fe^0$ through H bonding and electron-acceptor-acceptor interaction, respectively. Meanwhile, N containing groups, methyl groups, C=O, and aromatic skeletal C=C groups in OTC or CAP were adsorbed by $C/Fe_3C/Fe^0$. The ESR spectra suggested that $^{\cdot}OH$ could degrade OTC and CAP, while $^1O_2$ presented selective oxidation to OTC. The degradation of OTC by $C/Fe_3C/Fe^0$ was faster and more effective as compared to that for Fe^0 alone. The weak degradation of CAP only occurred on the surface of $C/Fe_3C/Fe^0$. The mechanistic and quantitative understanding of adsorption and degradation provided a theoretical basis for the application of this system without purging O_2 or adding H_2O_2. $C/Fe_3C/Fe^0$ exhibited excellent recycling capacity and could be used continuously. The $C/Fe_3C/Fe^0$ composite was very stable with little iron leaching to avoid secondary pollution, which was a promising material for the treatment of antibiotics-rich industrial wastewater.

CRediT authorship contribution statement

Nan Zhao: Methodology, Investigation, Data curation, Writing - original draft. **Kunyuan Liu:** Investigation, Data curation, Formal analysis. **Chao He:** Writing - review & editing. **Jia Gao:** Investigation, Data curation, Formal analysis. **Weihua Zhang:** Conceptualization, Writing - review & editing. **Tingjie Zhao:** Investigation, Data curation,

Formal analysis. **Daniel C.W. Tsang:** Writing - review & editing. **Rongliang Qiu:** Conceptualization, Writing - review & editing, Supervision.

Declaration of Competing Interest

The authors declare that they have no known competing financial interests or personal relationships that could have appeared to influence the work reported in this paper.

Acknowledgements

This project is supported by National Key Research and Development Program of China (2018YFD0800700), National Natural Science Foundation of China (41807113), Natural Science Foundation of Guangdong Province (2018A030313940), Fundamental Research Funds for the Central Universities (18lgpy46) and the 111 project (B18060).

Appendix A. Supplementary data

Supplementary data to this article can be found online at https://doi.org/10.1016/j.envint.2020.105899.

References

Ahmed, M.B., Zhou, J.L., Ngo, H.H., Guo, W.S., Johir, M.A., Belhaj, D., 2017a. Competitive sorption affinity of sulfonamides and chloramphenicol antibiotics toward functionalized biochar for water and wastewater treatment. Bioresour. Technol. 238, 306–312.

Ahmed, M.B., Zhou, J.L., Ngo, H.H., Guo, W.S., Johir, M.A.H., Sornalingam, K., Belhaj, D., Kallel, M., 2017b. Nano-Fe^0 immobilized onto functionalized biochar gaining excellent stability during sorption and reduction of chloramphenicol via transforming to reusable magnetic composite. Chem. Eng. J. 322, 571–581.

Bi, W.L., Wu, Y.L., Wang, X.N., Zhai, P.P., Dong, W.B., 2016. Degradation of oxytetracycline with $SO_4^{\cdot-}$ under simulated solar light. Chem. Eng. J. 302, 811–818.

Bokare, A.D., Choi, W.Y., 2015. Singlet-oxygen generation in alkaline periodate solution. Environ. Sci. Technol. 49, 14392–14400.

Chen, B.L., Chen, Z.M., Lv, S.F., 2011. A novel magnetic biochar efficiently sorbs organic pollutants and phosphate. Bioresour. Technol. 102 (2), 716–723.

Chen, H.L., Peng, Y.P., Chen, K.F., Lai, C.H., Lin, Y.C., 2016. Rapid synthesis of Ti-MCM-41 by microwave-assisted hydrothermal method towards photocatalytic degradation of oxytetracycline. J. Environ. Sci. 44, 76–87.

Chen, J.F., Yang, Y.W., Liu, Y.Y., Tang, M.Z., Wang, R.J., Tian, Y.P., Jia, C.X., 2019. Bacterial community shift and antibiotics resistant genes analysis in response to biodegradation of oxytetracycline in dual graphene modified bioelectrode microbial fuel cell. Bioresour. Technol. 276, 236–243.

Devi, P., Saroha, A.K., 2015. Simultaneous adsorption and dechlorination of pentachlorophenol from effluent by Ni-ZVI magnetic biochar composites synthesized from paper mill sludge. Chem. Eng. J. 271, 195–203.

Efimov, M.N., Vasilev, A.A., Chernikova, E.V., Toms, R.V., Muratov, D.G., Pankina, G.V., Chernavskii, P.A., Karpacheva, G.P., 2018. Polyacrylonitrile molecular weight effect on the structural and magnetic properties of metal-arbon nanomaterial. Mendeleev Commun. 28 (5), 556–558.

Erdim, E., Badireddy, A.R., Wiesner, M.R., 2015. Characterizing reactive oxygen generation and bacterial inactivation by a zerovalent iron-fullerene nano-composite device at neutral pH under UV-A illumination. J. Hazard. Mater. 380 (283), 80–88.

Fernandes, M.R.C., Huang, X.M., Abbenhuis, H.C.L., Hensen, E.J.M., 2019. Lignin oxidation with an organic peroxide and subsequent aromatic ring opening. Int. J. Biol. Macromol. 123, 1044–1051.

Grosvenor, A.P., Kobe, B.A., Biesinger, M.C., Mcintyre, N.S., 2004. Investigation of multiplet splitting of Fe 2p XPS spectra and bonding in iron compounds. Surf. Interf. Anal. 36 (12), 1564–1574.

Guan, X.H., Sun, Y.K., Qin, H.J., Li, J.X., Lo, I.M.C., He, D., Dong, H.R., 2015. The limitations of applying zero-valent iron technology in contaminants sequestration and the corresponding countermeasures: the development in zero-valent iron technology in the last two decades (1994–2014). Water Res. 75, 224–248.

Harada, T., Yatagai, T., Kawase, Y., 2016. Hydroxyl radical generation linked with iron dissolution and dissolved oxygen consumption in zero-valent iron wastewater treatment process. Chem. Eng. J. 303, 611–620.

Hsu, L.C., Liu, Y.T., Syu, C.H., Huang, M.H., Tzou, Y.M., Teah, H.Y., 2018. Adsorption of tetracycline on Fe (hydr)oxides: effects of pH and metal cation (Cu^{2+}, Zn^{2+} and Al^{3+}) addition in various molar ratios. Roy. Soc. Open Sci. 5, 171941.

Jiang, L., Hu, X.L., Yin, D.Q., Zhang, H.C., Yu, Z.Y., 2011. Occurrence, distribution and seasonal variation of antibiotics in the Huangpu River, Shanghai, China. Chemosphere 82 (6), 822–828.

Jo, W.-K., Kumar, S., Isaacs, M.A., Lee, A.F., Karthikeyan, S., 2017. Cobalt promoted TiO_2/GO for the photocatalytic degradation of oxytetracycline and congo red. Appl. Catal. B Environ. 201, 159–168.

Kemper, N., 2008. Veterinary antibiotics in the aquatic and terrestrial environment. Ecol. Ind. 8 (1), 1–13.

Kolpin, D.W., Furlong, E.T., Meyer, M.T., Thurman, E.M., Zaugg, S.D., Barber, L.B., Buxton, H.T., 2002. Pharmaceuticals, hormones, and other organic wastewater contaminants in US streams, 1999–2000: a national reconnaissance. Environ. Sci. Technol. 36 (6), 1202–1211.

Lei, C., Sun, Y., Khan, E., Chen, S.S., Tsang, D.C.W., Graham, N.J.D., Ok, Y.S., Yang, X., Lin, D., Feng, Y., Li, X.D., 2018a. Removal of chlorinated organic solvents from hydraulic fracturing wastewater by bare and entrapped nanoscale zero-valent iron. Chemosphere 196, 9–17.

Lei, C., Sun, Y., Tsang, D.C.W., Lin, D., 2018b. Environmental transformations and ecological effects of iron-based nanoparticles. Environ. Pollut. 232, 10–30.

Li, C., Luo, F., Duan, H.J., Dong, F.L., Chen, X.Y., Feng, M.B., Zhang, Z.R., Cizmas, L., Sharma, V.K., 2019a. Degradation of chloramphenicol by chlorine and chlorine dioxide in a pilot-scale water distribution system. Sep. Purif. Technol. 211, 564–570.

Li, H., Chen, S., Ren, L.Y., Zhou, L.Y., Tan, X.J., Zhu, Y., Belver, C., Bedia, J., Yang, J., 2019b. Biochar mediates activation of aged nanoscale ZVI by *Shewanella putrefaciens* CN32 to enhance the degradation of Pentachlorophenol. Chem. Eng. J. 368, 148–156.

Li, Z., Sun, Y., Yang, Y., Han, Y., Wang, T., Chen, J., Tsang, D.C.W., 2020. Biochar-supported nanoscale zero-valent iron as an efficient catalyst for organic degradation in groundwater. J. Hazard. Mater. 383, 121240.

Liao, P., Zhan, Z.Y., Dai, J., Wu, X.H., Zhang, W.B., Wang, K., Yuan, S.H., 2013. Adsorption of tetracycline and chloramphenicol in aqueous solutions by bamboo charcoal: a batch and fixed-bed column study. Chem. Eng. J. 228, 496–505.

Lindsey, M.E., Meyer, M., Thurman, E.M., 2001. Analysis of trace levels of sulfonamide and tetracycline antimicrobials, in groundwater and surface water using solid-phase extraction and liquid chromatography/mass spectrometry. Anal. Chem. 73 (19), 4640–4646.

Liu, B., Yao, H.Q., Daniels, R.A., Song, W.Q., Zheng, H.Q., Jin, L., Suib, S.L., He, J., 2016. A facile synthesis of Fe_3C@mesoporous carbon nitride nanospheres with superior electrocatalytic activity. Nanoscale 8 (10), 5441–5445.

Liu, X.Y., Huang, F., He, Y.D., Yu, Y., Lv, Y., Xu, Y.H., Zhang, Y.J., 2019. Oxytetracycline degradation and toxicity evolution by catalytic oxidation process over sludge derived carbon. J. Environ. Chem. Eng. 7, 102889.

Luo, J.W., Li, X., Ge, C.J., Muller, K., Yu, H.M., Huang, P., Li, J.T., Tsang, D.C.W., Bolan, N.S., Rinklebe, J., Wang, H.L., 2018. Sorption of norfloxacin, sulfamerazine and oxytetracycline by KOH-modified biochar under single and ternary systems. Bioresour. Technol. 263, 385–392.

Mao, Q.M., Zhou, Y.Y., Yang, Y., Zhang, J.C., Liang, L.F., Wang, H.L., Luo, S., Luo, L., Jeyakumar, P., Ok, Y.S., Rizwan, M., 2019. Experimental and theoretical aspects of biochar-supported nanoscale zerovalent iron activating H_2O_2 for ciprofloxacin removal from aqueous solution. J. Hazard. Mater. 380, 120848.

Misra, T., Mitra, S., Sen, S., 2018. Adsorption studies of carbamazepine by green-synthesized magnetic nanosorbents. Nanotechnol. Environ. Eng. 3, 11.

Navada, K.K., Kulal, A., 2019. Enzymatic degradation of chloramphenicol by laccase from *Trametes hirsuta* and comparison among mediators. Int. Biodeter. Biodegr. 138, 63–69.

Oliveira, V.D., Neri, R.C.D., Do Monte, F.T.D., Roberto, N.A., Costa, H.M.S., Assis, C.R.D., Santos, J.F., Bezerra, R.S., Porto, A.L.F., 2019. Crosslink-free collagen from *Cichla ocellaris*: structural characterization by FT-IR spectroscopy and densitometric evaluation. J. Mol. Struct. 1176, 751–758.

Park, M.H., Lee, J., Kim, J.Y., 2019. Oxidation resistance of nanoscale zero-valent iron supported on exhausted coffee grounds. Chemosphere 234, 179–186.

Rayaroth, M.P., Prasanthkumar, K.P., Kang, Y.G., Lee, C.S., Chang, Y.S., 2019. Degradation of carbamazepine by singlet oxygen from sulfidized nanoscale zero-valent iron – citric acid system. Chem. Eng. J. 382, 122828.

Shen, W., Kang, H., Ai, Z., 2018. Comparison of aerobic atrazine degradation with zero valent aluminum and zero valent iron. J. Hazard. Mater. 357, 408–414.

Sun, Y.Q., Yu, I.K.M., Tsang, D.C.W., Cao, X.D., Lin, D.H., Wang, L.L., Graham, N.J.D., Alessi, D.S., Komarek, M., Ok, Y.S., Feng, Y.J., Li, X.D., 2019. Multifunctional iron-biochar composites for the removal of potentially toxic elements, inherent cations, and hetero-chloride from hydraulic fracturing wastewater. Environ. Int. 124, 521–532.

Szymanska, U., Wiergowski, M., Soltyszewsk, I., Kuzemko, J., Wiergowska, G., Wozniak, M.K., 2019. Presence of antibiotics in the aquatic environment in Europe and their analytical monitoring: Recent trends and perspectives. Microchem. J. 147, 729–740.

Tiwari, D., Bhunia, H., Bajpai, P.K., 2018. Development of chemically activated N-enriched carbon adsorbents from urea-formaldehyde resin for CO_2 adsorption: kinetics, isotherm, and thermodynamics. J. Environ. Manage. 218, 579–592.

Vollprecht, D., Krois, L.M., Sedlazeck, K.P., Muller, P., Mischitz, R., Olbrich, T., Pomberger, R., 2019. Removal of critical metals from waste water by zero-valent iron. J. Cleaner Prod. 208, 1409–1420.

Wang, D.X., Liu, L.L., Jiang, X.Y., Yu, J.G., Chen, X.H., Chen, X.Q., 2015. Adsorbent for *p*-phenylenediamine adsorption and removal based on graphene oxide functionalized with magnetic cyclodextrin. Appl. Surf. Sci. 329, 197–205.

Wang, Q., Yates, S.R., 2008. Laboratory study of oxytetracycline degradation kinetics in animal manure and soil. J. Agr. Food Chem. 56, 1683–1688.

Wu, Y.W., Yue, Q.Y., Ren, Z.F., Gao, B.Y., 2018. Immobilization of nanoscale zero-valent iron particles (nZVI) with synthesized activated carbon for the adsorption and degradation of Chloramphenicol (CAP). J. Mol. Liq. 262, 19–28.

Xiao, J.N., Yue, Q.Y., Gao, B.Y., Sun, Y.Y., Kong, J.J., Gao, Y., Li, Q., Wang, Y., 2014. Performance of activated carbon/nanoscale zero-valent iron for removal of trihalomethanes (THMs) at infinitesimal concentration in drinking water. Chem. Eng. J. 253, 63–72.

Xu, J., Bian, Z.Y., Xin, X., Chen, A., Wang, H., 2018. Size dependence of nanosheet $BiVO_4$ with oxygen vacancies and exposed 001 facets on the photodegradation of oxytetracycline. Chem. Eng. J. 337, 684–696.

Xu, J., Liu, X., Cao, Z., Bai, W., Shi, Q., Yang, Y., 2020. Fast degradation, large capacity, and high electron efficiency of chloramphenicol removal by different carbon-supported nanoscale zerovalent iron. J. Hazard. Mater. 384, 121253. https://doi.org/10.1016/j.jhazmat.2019.121253.

Yan, Q.G., Wan, C.X., Liu, J., Gao, J.S., Yu, Fei, Zhang, J.L., Cai, Z.Y., 2013. Iron nanoparticles *in situ* encapsulated in biochar-based carbon as an effective catalyst for the conversion of biomass-derived syngas to liquid hydrocarbons. Green Chem. 15, 1631.

Yang, Y., Xu, L., Li, W., Fan, W., Song, S., Yang, J., 2019. Adsorption and degradation of sulfadiazine over nanoscale zero-valent iron encapsulated in three-dimensional graphene network through oxygen-driven heterogeneous Fenton-like reactions. Appl. Catal. B Environ. 259, 118057.

Yao, B., Liu, Y.Z., Zou, D.L., 2019. Removal of chloramphenicol in aqueous solutions by modified humic acid loaded with nanoscale zero-valent iron particles. Chemosphere 226, 298–306.

Zeng, Q.X., Xu, G.C., Zhang, L., Lin, H., Lv, Y., Jia, D.J., 2018. Porous CuO nanofibers derived from a Cu-based coordination polymer as a photocatalyst for the degradation of rhodamine B. New J. Chem. 42, 7016–7024.

Zhao, H., Qian, L., Chen, Y., Wang, Q., Zhao, G., 2018. Selective catalytic two-electron O_2 reduction for onsite efficient oxidation reaction in heterogeneous electro-fenton process. Chem. Eng. J. 332, 486–498.

Zhao, N., Chang, F., Hao, B., Yu, L., Morel, J.L., Zhang, J., 2019. Removal of organic dye by biomass-based iron carbide composite with an improved stability and efficiency. J. Hazard. Mater. 369, 621–631.

Zhao, N., Yang, X.X., Zhang, J., Zhu, L., Lv, Y.Z., 2017a. Adsorption mechanisms of dodecylbenzene sulfonic acid by corn straw and poplar leaf biochars. Materials 10 (10).

Zhao, N., Zhao, C.F., Lv, Y.Z., Zhang, W.F., Du, Y.G., Hao, Z.P., Zhang, J., 2017b. Adsorption and coadsorption mechanisms of Cr(VI) and organic contaminants on H_3PO_4 treated biochar. Chemosphere 186, 422–429.

Zhu, K.R., Xu, H., Chen, C.L., Ren, X.M., Alsaedi, A., Hayat, T., 2019. Encapsulation of Fe^0-dominated $Fe_3O_4/Fe^0/Fe_3C$ nanoparticles into carbonized polydopamine nanospheres for catalytic degradation of tetracycline via persulfate activation. Chem. Eng. J. 372, 304–311.